

A High-Rate and Ultrastable Sodium Ion Anode Based on a Novel $\text{Sn}_4\text{P}_3\text{-P}$ at Graphene Nanocomposite

Xu, Yaolin; Peng, Bo; Mulder, Fokko M.

DOI

[10.1002/aenm.201701847](https://doi.org/10.1002/aenm.201701847)

Publication date

2017

Document Version

Final published version

Published in

Advanced Energy Materials

Citation (APA)

Xu, Y., Peng, B., & Mulder, F. M. (2017). A High-Rate and Ultrastable Sodium Ion Anode Based on a Novel $\text{Sn}_4\text{P}_3\text{-P}$ at Graphene Nanocomposite. *Advanced Energy Materials*, 8 (2018)(3), Article 1701847. <https://doi.org/10.1002/aenm.201701847>

Important note

To cite this publication, please use the final published version (if applicable). Please check the document version above.

Copyright

Other than for strictly personal use, it is not permitted to download, forward or distribute the text or part of it, without the consent of the author(s) and/or copyright holder(s), unless the work is under an open content license such as Creative Commons.

Takedown policy

Please contact us and provide details if you believe this document breaches copyrights. We will remove access to the work immediately and investigate your claim.

A High-Rate and Ultrastable Sodium Ion Anode Based on a Novel Sn₄P₃-P@Graphene Nanocomposite


Yaolin Xu, Bo Peng, and Fokko M. Mulder*

Phosphorus and tin phosphide based materials that are extensively researched as the anode for Na-ion batteries mostly involve complexly synthesized and sophisticated nanocomposites limiting their commercial viability. This work reports a Sn₄P₃-P (Sn:P = 1:3) @graphene nanocomposite synthesized with a novel and facile mechanochemical method, which exhibits unrivalled high-rate capacity retentions of >550 and 371 mA h g⁻¹ at 1 and 2 A g⁻¹, respectively, over 1000 cycles and achieves excellent rate capability (>815, ≈585 and ≈315 mA h g⁻¹ at 0.1, 2, and 10 A g⁻¹, respectively).

Na-ion batteries recently have received increasing research attention as an alternative to Li-ion batteries due to the higher abundance and thus much lower cost of Na resources compared to Li.^[1–5] Phosphorus^[6–14] and tin^[15–23] have been intensively investigated as the anode materials for Na-ion batteries due to their high capacities upon alloying with Na (Na₃P: 2596 mA h g⁻¹, Na₁₅Sn₄: 847 mA h g⁻¹). However, the electronic conductivity of phosphorus is low (10⁻¹⁴ S cm⁻¹ for red P); and these alloying reactions are inevitably accompanied with substantial volume expansions (volume change of 490% from P to Na₃P^[12] and 525% from Sn to Na₁₅Sn₄^[17]), and with drastic structural collapse when Na ions are extracted. As a result, upon repetitive dis-/charge, it undergoes irreversible and adverse pulverization of active materials and loss of electrical conduction and eventually the battery failure. To address these issues, various designs of nanostructured Sn/P–C composites have been reported,^[7–14,18–23] but the manufacturing cost is still to be reduced and the achieved reversible sodiation capacity is still to be improved. Very recently, Li et al.^[14] demonstrated a red P@MOF (metal-organic framework) derived N-doped microporous carbon exhibiting a capacity of 450 mA h g⁻¹ at 1 A g⁻¹ after 1000 cycles. Sha et al.^[23] fabricated Sn nanoparticles@N-doped carbon nanofiber which achieved a capacity of 390 mA h g⁻¹ at 0.847 A g⁻¹ over 1000 cycles.

Y. Xu, Dr. B. Peng, Prof. F. M. Mulder
Materials for Energy Conversion and Storage (MECS)
Department of Chemical Engineering
Faculty of Applied Science
Delft University of Technology
Van der Maasweg 9, 2629 HZ Delft, The Netherlands
E-mail: f.m.mulder@tudelft.nl

Dr. B. Peng
Department of Physics
Renmin University of China
No. 59 Zhongguancun Street, Haidian District, Beijing 100872, China

 The ORCID identification number(s) for the author(s) of this article can be found under <https://doi.org/10.1002/aenm.201701847>.

DOI: 10.1002/aenm.201701847

Metal phosphides (MP_x, M = Ni,^[24] Cu,^[25,26] Ge,^[27,28] Fe,^[29,30] Sn,^[31–41] etc.) have also shown high reversible capacities for Na ion storage and much improved cycling stability and rate capability, which originates from the enhancement of electrical conductivity upon the presence of metal atoms as electronic pathways for phosphorus atoms. Among all these metal phosphides, SnP_x received the most research attention. Fan et al.^[31] reported a SnP₃/C nanocomposite Na ion

anode delivering a capacity of ≈810 mA h g⁻¹ at 0.15 A g⁻¹ in 150 cycles. Usui et al.^[32] showed that Sn₄P₃ exhibits a much enhanced electrochemical cycling performance of reversible Na ion storage compared to SnP₃ due to its superior electronic conductivity and more uniform Sn dispersion in the P matrix. Liu et al.^[36] synthesized yolk-shell Sn₄P₃@C nanospheres which achieved a reversible capacity retention of 360 mA h g⁻¹ for Na ion storage at 1.5 A g⁻¹ after 400 cycles. However, long-term cycling of more than 500 cycles with a high stability and high reversible capacity for Na ion storage has not been reported.

In this work, a nanocomposite of Sn₄P₃ and phosphorus (Sn:P = 1:3) embedded in a graphene matrix has been synthesized via a novel mechanochemical transformation method. This composite exhibits an ultrastable and much improved capacity retention at a high current rate (>550 mA h g⁻¹ in 1000 cycles at 1 A g⁻¹) and unrivalled rate capability (>815 mA h g⁻¹ at 0.1 A g⁻¹, ≈585 mA h g⁻¹ at 2 A g⁻¹, and ≈315 mA h g⁻¹ at 10 A g⁻¹). This is, to the best of our knowledge, superior to any other Sn–P compounds and other metal phosphides based materials reported as the anode for Na-ion batteries and it provides substantial promise to its practical applications in Na-ion batteries that typically require at least 1000 cycles.

As described in **Figure 1a** (see the details in the Experimental Section), the Sn₄P₃-P@graphene nanocomposite (indicated as SPPG) is synthesized via mechanochemical transformation from the SnP₃@graphene composite (indicated as SPG) (reaction (1))



where SnP₃ is initially mechanochemically synthesized from Sn and red P (reaction (2))



The initial formation of SnP₃ is evidenced by X-ray diffraction (XRD) (Figure 1b; Figure S1, Supporting Information) as all the peaks can be indexed to the SnP₃ phase (Pearson's Crystal Data (PCD) #1250771, space group: *R-3mh*). It is

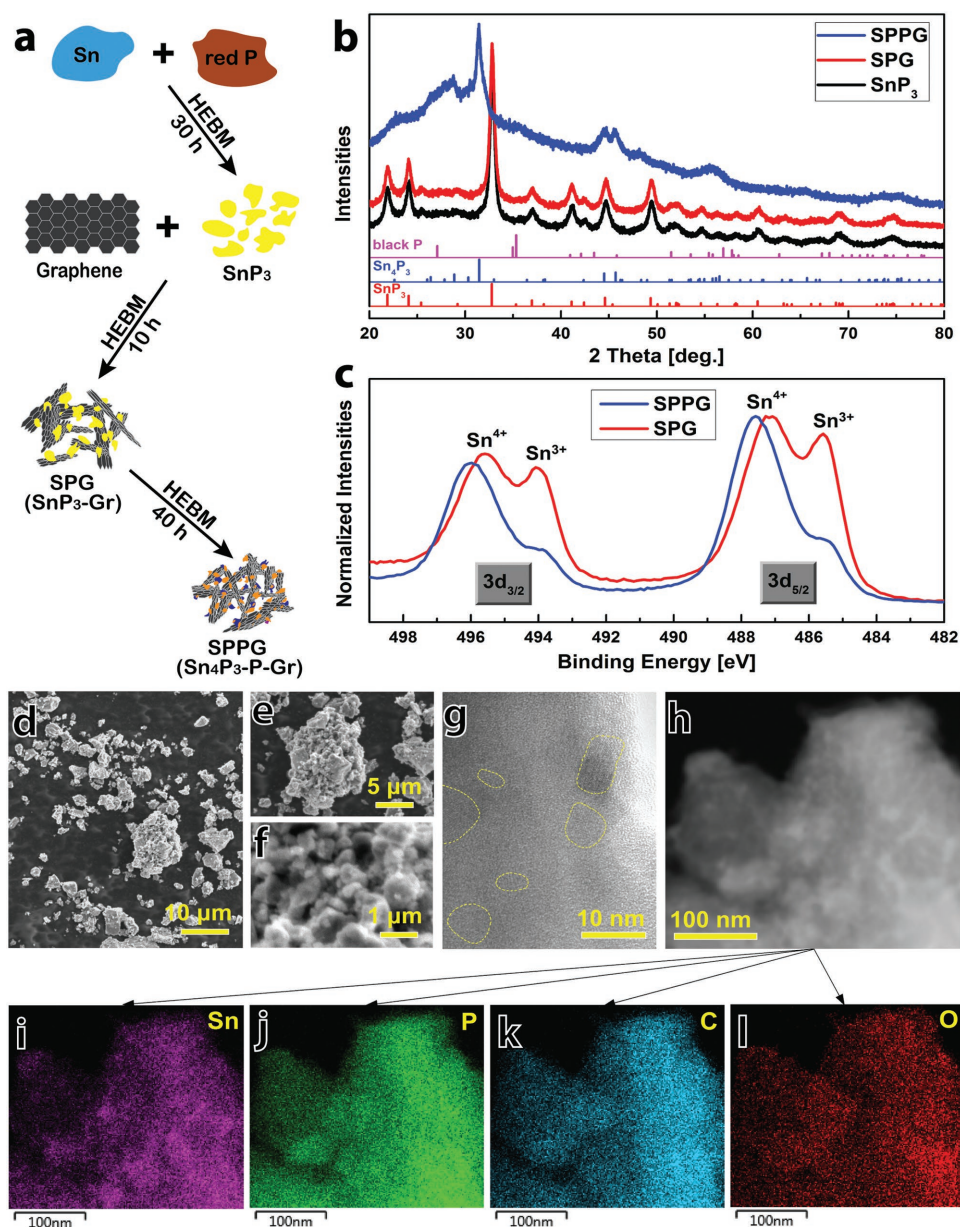


Figure 1. Sample synthesis and characterization. a) A schematic of the mechanochemical synthesis process (HEBM: high energy ball milling). b) XRD patterns of the samples (reference patterns from Pearson's Crystal Data (PCD) database: SnP_3 : PCD#1250771, space group: $R\text{-}3mh$; Sn_4P_3 : PCD#1910451, space group: $R\text{-}3mh$; black P: PCD#1214640, space group: $Cmce$). c) XPS spectra of the SPPG and SPG samples. d–f) SEM images of the SPPG sample at different magnifications. g) High-resolution TEM image of the SPPG sample. h) ADF-STEM image of the SPPG sample and the STEM-EDX element mapping of i) Sn and j) P, k) C, and l) O, respectively.

retained after a short-term mechanical milling with graphene, and is mechanochemically converted to Sn_4P_3 (PCD#1910451, space group: $R\text{-}3mh$) when further milling is performed as is observed by XRD (Figure 1b). Rietveld refinement on the XRD patterns (Figure S2 and Table S1, Supporting Information) show that the average crystalline domain size of SnP_3 amounts to 15.0 nm, while that of Sn_4P_3 is much reduced to 9.4 nm due to the refinement effect of high energy mechanical milling.

The conversion from SnP_3 to Sn_4P_3 is also evident in the X-ray Photoelectron Spectroscopy (XPS) investigation (Figure 1c; Figure S3, Supporting Information). In the analysis of Sn 3d

XPS spectra of Sn–P compounds, multiple valence contributions (Sn^{2+} , Sn^{4+} , etc.) are generally considered.^[34,39,40,42] SnP_3 has a single Sn site surrounded by six P atoms in the crystal structure and a ^{119}Sn Mössbauer Isomer shift indicates an oxidation state of +3 in bulk crystals,^[43] the main Sn $3d_{5/2}$ XPS peak of SnP_3 at 485.5 eV may therefore be assigned to Sn^{3+} . The higher binding energy peak at 487.2 eV results from oxidized Sn^{4+} on the surface of nanoparticles. Such high oxidation occurs likely because of the P surface termination leading to a higher Sn oxidation state. It should also be noted that some unavoidable surface oxidation by oxygen may be present,

which is consistent with the peaks of P–O bonds in the P 2p spectra, and also in line with other XPS studies on Sn–P compounds.^[31,34,42] However, since the P terminated surface already leads to the oxidation of Sn to +4, the oxidizing effect of oxygen on Sn may be limited. The strong peak of SPPG at 487.6 eV has a line width and shape similar to the spectrum of Sn₄P₃ in refs. [34,39] and [40], and the weak peak at 485.5 eV may indicate a small fraction of remaining SnP₃. The valence of Sn is suggested by the Mössbauer study^[43] to be lower in Sn₄P₃ compared to SnP₃, and may be +2.25 on average assuming a chemical state of P³⁻. The XPS binding energies depend on local coordination as well as valence, and 1–2 eV deviations are usually observed in binding energies for the same valence depending on the coordination in the compounds.^[44] In Sn₄P₃, the Sn-1 atoms are octahedrally coordinated by six P atoms resembling SnP₃, whereas Sn-2 atoms have a [3+3] coordination consisting of three P and three Sn-2 atoms. Thus, the binding energy will deviate from that in SnP₃ and shift to higher binding energies. Meanwhile, a Sn⁴⁺ contribution cannot be excluded for the same reason of surface termination by P.

In the SPPG sample, phosphorus is formed and embedded in the graphene matrix and it appears as black phosphorus (PCD#1214640, space group: *Cmce*) but is poorly crystalline; weak but distinguishable peaks at 27.0° and ≈35.0° can be observed in the XRD pattern of SPPG corresponding to the Bragg diffraction on the lattice planes (021) and (040)/(111) of black phosphorus, respectively. Scanning electron microscope (SEM) images (Figure 1d–f) show that the SPPG nanocomposite appears as agglomerations of nanoparticles and SEM based energy dispersive X-ray spectroscopy (EDX) element mapping on the agglomeration (Figure S4, Supporting Information) reports a homogeneous distribution of P and Sn in the composite. Transmission electron microscope (TEM) images (Figure 1g; Figure S5, Supporting Information) and the annular dark field (ADF) scanning transmission electron microscope (STEM) image (Figure 1h) show the nanosized crystalline domains of active materials embedded in the graphene matrix and distributed evenly; and the STEM-EDX based element mapping of Sn (Figure 1i) shows a consistent distribution with the distribution of active materials in the ADF-STEM image. P appears not only where Sn is concentrated but uniformly throughout the sample, and so do C and O (Figure 1j–l), which reveals that elemental phosphorus formed in reaction (1) distributes homogeneously within the graphene network. Therefore, taking into account the poor crystallinity of black phosphorus and small crystalline domain size of Sn₄P₃, black phosphorus and Sn₄P₃ would appear as nanocrystallites next to each other, well dispersed in the graphene matrix, thanks to the presence of graphene which alleviates the aggregation issues upon their formation during the mechanical milling. Moreover, strong interactions between the active materials and graphene can be present in the sample. For instance, the presence of P–O–C bond in the sample is evident (Figure S3, Supporting Information) induced by the strong mechanical milling, which are also evidenced in many other phosphorus/metal phosphides–carbon systems.^[25,28,45–47]

The transformation in reaction (1) upon the presence of graphene is interesting since neither C–P nor C–Sn binary compounds exist in bulk.^[48] However, carbon–phosphorus

composites can be formed in which element carbon and phosphorus are intermixed on a nanoscale,^[7,49] apparently stabilized by abundant interface reactions. The presence of carbon (graphene) in the Sn–P–C system apparently likewise enables the formation of a relatively stable C–black P composite during the high energy ball milling, which enables the transformation from SnP₃ to Sn₄P₃ with the stabilization of P in the composite being the main factor.

The electrochemical performance of the samples for Na ion storage has been characterized in half-cell Na-ion batteries and the capacity is calculated based on the mass of Sn and P (excl. graphene) considering the lower mass ratio of graphene in the composites and its negligible capacity for Na ion uptake (Figure S6, Supporting Information).

Figure 2a demonstrates that SPPG exhibits an initial desodiation capacity of 708 mA h g⁻¹ at 0.4 A g⁻¹, which gradually grows to 855 mA h g⁻¹ in 100 cycles and then drops to ≈800 mA h g⁻¹ in 200 cycles and keeps stable after that. A capacity of 796 mA h g⁻¹ can be achieved after 300 cycles. The Coulombic efficiency is 73.1% at the 1st cycle and jumps to 96.2% at the 2nd cycle, and it reaches >99.5% within 20 cycles and keeps stable afterward. In comparison, SPG also undergoes an initial capacity growth for Na ion uptake and achieves 714 mA h g⁻¹ after 70 cycles and then stays stable; the Coulombic efficiency increases to 98.9% within 20 cycles and is stabilized afterward. However, the capacity drops gradually after 130 cycles and a capacity of only 546 mA h g⁻¹ is retained in 300 cycles. In addition, the SnP₃ (without graphene) based electrode obtains an initial desodiation capacity of 671 mA h g⁻¹ which is comparable with SPPG and SPG, but deteriorates rapidly along cycling. The capacity retention drops to <90 mA h g⁻¹ in 100 cycles. Figure 2b shows that the desodiation capacity of SPPG reaches >815 mA h g⁻¹ at 0.1 A g⁻¹ and a capacity of ≈705, ≈585, and ≈315 mA h g⁻¹ can be achieved when the current rate increases to 0.2, 2, and 10 A g⁻¹, respectively. A capacity of >810 mA h g⁻¹ can be restored when the current rate is reset at 0.1 A g⁻¹ indicating its excellent rate capability. The rate performance of SPG for Na ion uptake follows a similar trend as SPPG but exhibits relatively lower capacities for Na ion storage.

It can be concluded, from the results in Figure 2a,b and Figure S7 (Supporting Information), that the capacity retention and cycling performance upgrade in the order of SnP₃ < SPG < SPPG, which can be associated with (i) more refined particle sizes induced by higher energy mechanical milling enabling faster kinetics for Na ion transport; (ii) better electrical conduction and alleviated volume expansion with the graphene matrix host and (iii) stronger interactions between the active materials and graphene which maintains the electrical conduction throughout the electrode along cycling; (iv) the higher intrinsic electronic conductivity of Sn₄P₃ than SnP₃.^[32]

The electrochemical performance of the SPPG based Na ion anode (Figure 2c) reports that cycling at a relatively lower current rate (0.2 and 0.4 A g⁻¹) a gradual improvement on the capacity is evidenced during the initial tens of cycles indicating an initial activation process, which is also observed in other reports.^[32,33,35] The desodiation capacity at 0.2 A g⁻¹ increases from 762 mA h g⁻¹ to 866 mA h g⁻¹ within 100 cycles and stays stable afterward, the retained capacity reaches 842 mA h g⁻¹ in

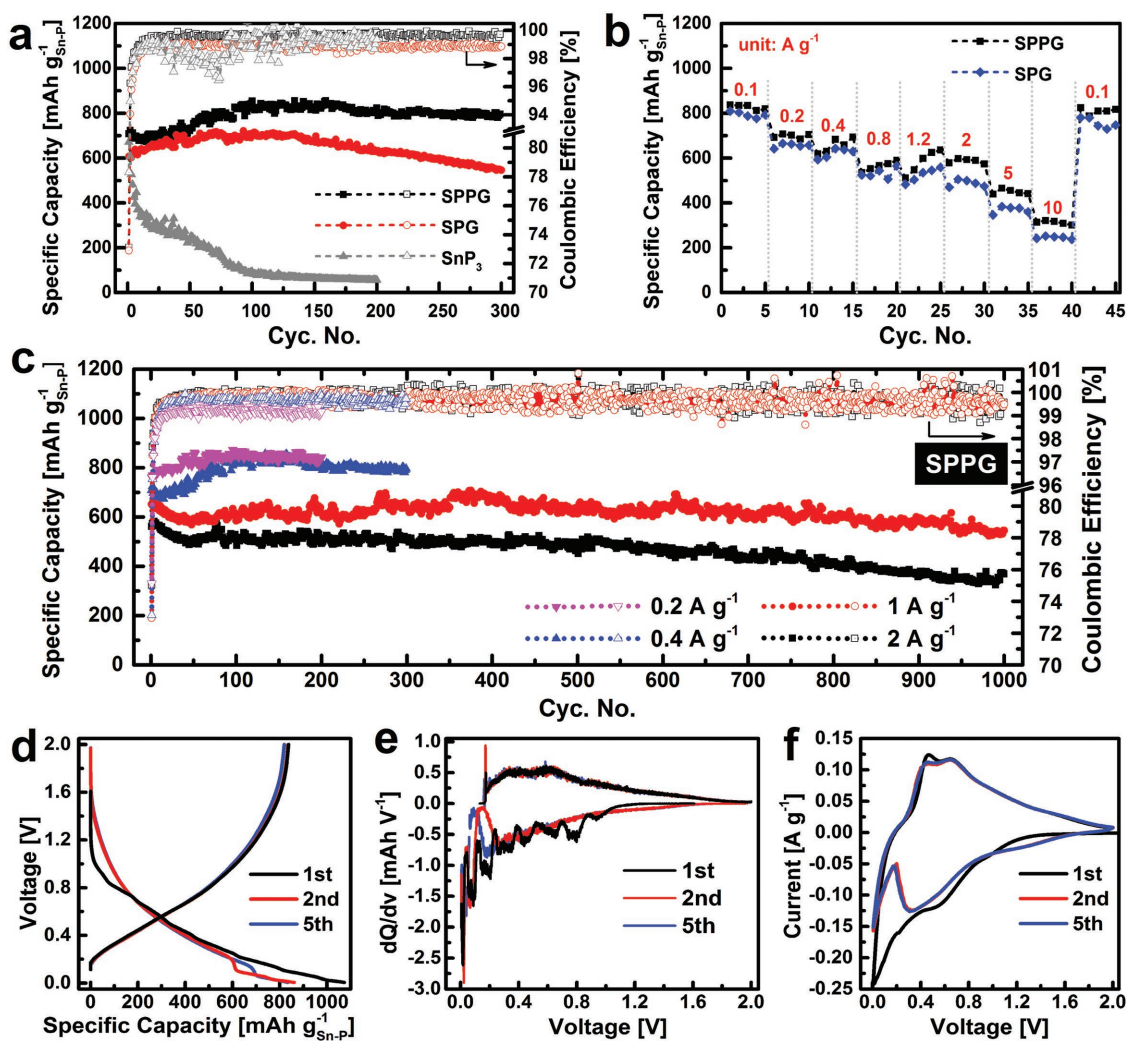


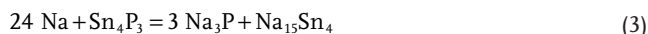
Figure 2. Electrochemical performance for Na ion uptake. a) Capacity retentions and Coulombic efficiencies of SPPG, SPG, and SnP₃ for Na ion uptake at 0.4 A g⁻¹. b) Rate capabilities of SPPG and SPG based Na ion anodes. c) Capacity retentions and Coulombic efficiencies for Na ion uptake in SPPG at different current rates: 0.2, 0.4, 1, and 2 A g⁻¹, respectively. d) Voltage profiles of the SPPG based Na ion anode at 0.2 A g⁻¹. e) Differential capacity (dQ/dV) plots for the SPPG anode reproduced from the voltage profiles shown in panel (d). f) Cyclic voltammograms of the SPPG anode (Scan rate: 0.5 mV s⁻¹).

200 cycles. The Coulombic efficiency is 75.1% and 96.3% for the 1st and 2nd cycle, respectively, and is stabilized at ≈99.2% from 30th cycle. In comparison, the activation process is not observed when the electrodes are dis-/charged at high current rates (1 and 2 A g⁻¹). Cycling at 1 A g⁻¹, the capacity of the SPPG based Na ion anode reaches 652 mA h g⁻¹ for the 1st cycle with a Coulombic efficiency of 73.0% which has increased to 97.3% in the 2nd cycle. The capacity retention deteriorates slightly in the initial 20 cycles and then stays extremely stable at ≈610 mA h g⁻¹ with a Coulombic efficiency >99.5%. A reversible capacity of 607 mA h g⁻¹ is achieved in 800 cycles after which a gentle degradation occurs but the retained capacity is still >550 mA h g⁻¹ after 1000 cycles. The initial reversible capacity at 2 A g⁻¹ is 561 mA h g⁻¹ and it undergoes a similar decreasing-stable-decreasing trend as observed at 1 A g⁻¹. The Coulombic efficiency reaches >99.5% within 15 cycles, and the retained capacity amounts to 512, 496, and 371 mA h g⁻¹ at 200th, 500th, and 1000th cycles, respectively. The minor

capacity fluctuations during the long-term cycling may result from the ambient temperature variations during cycling and have also been observed in other studies.^[31,33–36,39,40] To the best of our knowledge, the capacity retentions at such high current rates and the cycling stability that SPPG has achieved are unparalleled among all the Sn–P compounds based anode materials for Na-ion batteries.

The relatively lower initial Coulombic efficiency (73–75%) is due to the formation of irreversible solid electrolyte interphase (SEI) layers on the surface of the active materials, which mainly takes place in the 1st cycle and is negligible in the following cycles. This irreversible process occurs at a relatively higher voltage range as can be observed in the initial sodiation voltage profile (voltage plateau at ≈0.95 V in Figure 2d), which is also evidenced in the differential capacity (dQ/dV) curve (voltage peak at 0.95 V in Figure 2e)^[25] and the cyclic voltammogram (broad peak at ≈0.95 V in Figure 2f)^[11,12,32–34] of the SPPG based electrode during the 1st sodiation process.

The initial Na ion insertion in SPPG undergoes several stages (at 0.78, 0.65, 0.44, 0.31, 0.18, 0.08, and 0.02 V) as illustrated in the voltage profile (Figure 2d) and differential capacity curve (Figure 2e), which originates from the stepwise Na ion insertion in phosphorus and Sn₄P₃, and the voltage decreases with the increasing Na content in the electrode. Based on the previous reports on the Na ion storage in SnP₃,^[31] Sn₄P₃,^[32–41] Sn,^[50–54] and P^[55] and it is possible that the relatively higher sodiation voltage peaks (at 0.78, 0.31, and 0.08 V) originate from the step-by-step Na ion insertion in phosphorus with the formation of Na₃P₇, NaP, Na₃P, etc., and the relatively lower voltage peaks (at 0.65, 0.44, 0.18, and 0.02 V) correspond to the reduction of Sn₄P₃ with the formation of Sn (together with Na_xP), Na₄Sn₄, Na₉Sn₄, and Na₁₅Sn₄, etc. The complete sodiation reaction can be depicted as reaction (3)



During the desodiation process, two broad voltage peaks at 0.33 and 0.6 V can be observed which can be assigned to the Na ion extraction from the Na–Sn alloys and Na₃P, respectively (reactions (4) and (5))^[31–35,38–40]



This is similar to the reaction mechanism proposed by Usui et al.^[32] that, after initial sodiation forming Na₁₅Sn₄ and Na₃P, elemental Sn and P react individually with Na ions at different potential regions in the following cycles.

Ex Situ XRD patterns (Figure 3a) of the sodiated electrode show that the active materials have been amorphized when it is initially sodiated due to the substantial structural change upon a large amount of Na ion insertion. The active materials stay amorphous (or extremely small crystallites) when the Na ion is extracted as the phosphorus and Sn₄P₃ particles stay refined attributed to their presence within the graphene matrix, which is also consistent with the other studies.^[27,35,39,56] Meanwhile, the Sn 3d XPS spectrum of the desodiated SPPG electrode is similar to that of the pristine SPPG (Figure 3b), which indicates that Sn₄P₃ is reformed. (A detailed XPS analysis on the cycled SPPG electrode is in Figure S8 in the Supporting Information.) Based on the discussions above, a proposal on the sodiation mechanism in SPPG is illustrated in Figure 3c.

The ultrahigh cycling stability of the SPPG composite can be contributed from several factors: (1) Nanosized phosphorus and Sn₄P₃ are embedded in the conductive graphene matrix which prevents the segregation issues and keeps the active materials nanorefined, which allows for rapid kinetics for Na ion uptake. Meanwhile, the graphene matrix also works as a host to accommodate the large volume change upon Na ion

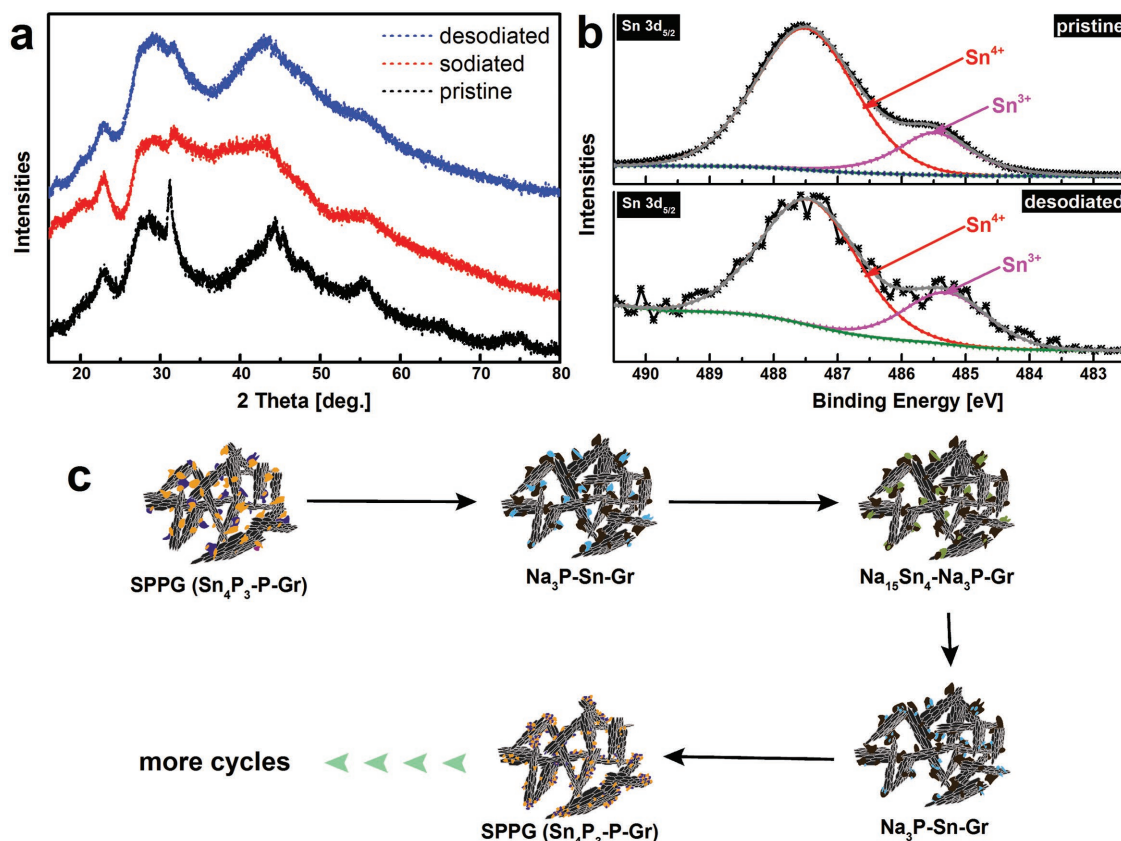


Figure 3. Mechanism of Na ion uptake in SPPG. a) Ex situ XRD spectra of the SPPG electrode at different stages. To avoid any unwanted peaks from the metal current collector, here the electrode is a thick self-supporting SPPG electrode (SPPG: PVDF: Super P carbon black = 7:1.5:1.5, ≈500 μm in thickness; details in the Supporting Information). b) XPS spectra of the pristine and desodiated SPPG electrode after dis-/charge for 20 cycles. c) A schematic illustration on the de-/sodiation mechanism in SPPG.

uptake. As a result, the structural integrity is retained over repetitive dis-/charge. (2) Upon the sodiation of P, less-conductive Na_3P is formed, which works as a shielding matrix for Sn atoms and prevents the aggregation issues; metallic Sn provides an electrical conduction pathway for Na_3P for reversible Na ion uptake. The complementary beneficial effects of Sn and Na_3P ultimately enhance the cycling performance.^[32,33,35,39,56] The high mobility of Na^+ in Na_3P ^[57] warrants an expedite expressway for Na ion transport throughout the active materials. (3) The strong interactions between the active materials and graphene (e.g., P—O—C bond) will maintain the electrical conduction between graphene and the active materials during cycling and thus enable a high cycling stability for Na ion storage. (4) A high Coulombic efficiency (>96%) in the 2nd cycle and growingly higher efficiencies in the following cycles (>99% within 10 cycles) have been observed indicating that the SEI formation almost stops after the 1st cycle as the initial compact NaF-dominant SEI layer protects the active materials from pulverization and further SEI formation^[31,34,37–39] and thus a stable cycling performance is achieved. In short, the structural integrity and electronic conduction of the electrode have been maintained along cycling and thus a high cycling stability has been achieved, which is also suggested by the SEM images (Figure S9, Supporting Information) and the electrochemical impedance spectroscopy measurement (Figure S10, Supporting Information) of the cycled SPPG electrodes.

In summary, this work presents a novel $\text{Sn}_4\text{P}_3\text{-P}$ (Sn:P = 1:3) @graphene nanocomposite mechanochemically transformed from SnP_3 @graphene. This composite exhibits a remarkably high and ultrastable capacity retention of >550 mA h g^{-1} over 1000 cycles at 1 A g^{-1} and unrivalled rate capability (>815 mA h g^{-1} at 0.1 A g^{-1} , \approx 585 mA h g^{-1} at 2 A g^{-1} and \approx 315 mA h g^{-1} at 10 A g^{-1}). This is, to the best of our knowledge, the best cycling stability and cycle life among all the reported Na ion anode materials based on Sn—P compounds, and it shows great promise for its practical applications in high energy density Na-ion batteries.

Experimental Section

Sample Synthesis: To synthesize SnP_3 , tin (Aldrich, <45 μm , 99.8%) and red phosphorus (Alfa Aesar, -325 mesh, 98.9%) powders were mixed with an atomic ratio of 1:3, then the mixture was mechanically milled for 30 h at 400 rpm with a ball to powder ratio of 100:1 under Ar atmosphere. Subsequently, the as-synthesized SnP_3 was mixed with graphene stacks (Cabot, ≈ 700 m^2 g^{-1}) with a mass ratio of 7:3 and then mechanically milled at the same conditions for 10 h to obtain the SPG sample or 50 h to get the SPPG nanocomposite.

Sample Characterization: XRD patterns were obtained with a PANalytical X'Pert Pro PW3040/60 diffractometer with a Cu K α source. The operating voltage and current were 45 kV and 40 mA, respectively. SEM images of the SPPG sample were obtained with a JEOL JSM 6010F scanning electron microscope working at an accelerating voltage of 5 kV. SEM-EDX based element mapping was carried out at an accelerating voltage of 20 kV. The TEM images and STEM-based EDX analysis were taken using a FEI-Tecnai with a field emission gun source working at 200 kV. XPS measurement was performed with a K-alpha Thermo Fisher Scientific spectrometer using a monochromatic Al K α source, and the spectra were analyzed with a Thermo Avantage software.

Electrode Preparation: The SPPG-, SPG-, and SnP_3 -based electrodes were prepared using a conventional slurry based method. Specifically,

the active materials, sodium carboxymethyl cellulose and super P carbon black are mixed with a mass ratio of 7:1:2 in deionized water until a homogeneous slurry was obtained; then the slurry was casted onto a piece of Cu foil (Goodfellow, 12.5 μm) and dried in a vacuum oven working at 70 $^\circ\text{C}$ for 12 h. Finally, the electrode was mechanically compacted with a roller compressor before it was cut into circular pieces for the final battery assembly. The mass loading of active materials is ≈ 0.5 mg cm^{-2} .

Electrochemistry: Na ion half-cells were assembled in an Ar atmosphere glove box ($\text{O}_2/\text{H}_2\text{O}$: <0.1 ppm). A sodium metal foil was employed as the counter electrode and a borosilicate micro glass fiber (Whatman) was used as the separator. The working electrolyte is 1 M NaClO_4 dissolved in ethylene carbonate and propylene carbonate ($v/v = 1:1$) with 10% fluoroethylene carbonate. The galvanostatic electrochemical performance was characterized with a MACCOR 4600 battery cycler. The cutoff voltages for sodiation and desodiation were 0.005 and 2 V versus Na/Na^+ , respectively. Cyclic voltammetry was carried out with a PGSTAT302N Autolab potentiostat within the same voltage range.

Supporting Information

Supporting Information is available from the Wiley Online Library or from the author.

Acknowledgements

This work was financially supported by the "A Green Deal in Energy Materials" (ADEM) grant funded by Dutch Ministry of Economic Affairs and ADEM industrial partners including Cabot/Norit. B.P. would like to thank the Chinese Scholarship Council (CSC) for financial support.

Conflict of Interest

The authors declare no conflict of interest.

Keywords

nanocomposites, Na-ion batteries, phosphorus, tin phosphide

Received: July 6, 2017

Revised: August 2, 2017

Published online: September 20, 2017

- [1] B. L. Ellis, L. F. Nazar, *Curr. Opin. Solid State Mater. Sci.* **2012**, *16*, 168.
- [2] H. Kim, H. Kim, Z. Ding, M. H. Lee, K. Lim, G. Yoon, K. Kang, *Adv. Energy Mater.* **2016**, *6*, 1600943.
- [3] W. Luo, F. Shen, C. Bommier, H. Zhu, X. Ji, L. Hu, *Acc. Chem. Res.* **2016**, *49*, 231.
- [4] X. Xiang, K. Zhang, J. Chen, *Adv. Mater.* **2015**, *27*, 5343.
- [5] K. Kubota, S. Komaba, *J. Electrochem. Soc.* **2015**, *162*, A2538.
- [6] W. L. H. X. Li Jiaoyang, *Prog. Chem.* **2016**, *28*, 193.
- [7] B. Peng, Y. Xu, K. Liu, X. Wang, F. M. Mulder, *ChemElectroChem* **2017**; <https://doi.org/10.1002/celc.201700345>.
- [8] G. L. Xu, Z. Chen, G. M. Zhong, Y. Liu, Y. Yang, T. Ma, Y. Ren, X. Zuo, X. H. Wu, X. Zhang, K. Amine, *Nano Lett.* **2016**, *16*, 3955.
- [9] C. Zhang, X. Wang, Q. Liang, X. Liu, Q. Weng, J. Liu, Y. Yang, Z. Dai, K. Ding, Y. Bando, J. Tang, D. Golberg, *Nano Lett.* **2016**, *16*, 2054.

- [10] Y. Zhu, Y. Wen, X. Fan, T. Gao, F. Han, C. Luo, S.-C. Liou, C. Wang, *ACS Nano* **2015**, 9, 3254.
- [11] S. Liu, J. Feng, X. Bian, J. Liu, H. Xu, Y. An, *Energy Environ. Sci.* **2017**, 10, 1222.
- [12] J. Qian, X. Wu, Y. Cao, X. Ai, H. Yang, *Angew. Chem.* **2013**, 125, 4731.
- [13] J. Zhou, X. Liu, W. Cai, Y. Zhu, J. Liang, K. Zhang, Y. Lan, Z. Jiang, G. Wang, Y. Qian, *Adv. Mater.* **2017**, 125, 1700214.
- [14] W. Li, S. Hu, X. Luo, Z. Li, X. Sun, M. Li, F. Liu, Y. Yu, *Adv. Mater.* **2017**, 29, 1605820.
- [15] Z. Li, J. Ding, D. Mitlin, *Acc. Chem. Res.* **2015**, 48, 1657.
- [16] M. Zhao, Q. Zhao, J. Qiu, H. Xue, H. Pang, *RSC Adv.* **2016**, 6, 95449.
- [17] J. W. Wang, X. H. Liu, S. X. Mao, J. Y. Huang, *Nano Lett.* **2012**, 12, 5897.
- [18] C. Kim, K.-Y. Lee, I. Kim, J. Park, G. Cho, K.-W. Kim, J.-H. Ahn, H.-J. Ahn, *J. Power Sources* **2016**, 317, 153.
- [19] Y. Xu, Y. Zhu, Y. Liu, C. Wang, *Adv. Energy Mater.* **2013**, 3, 128.
- [20] Y. Liu, N. Zhang, L. Jiao, Z. Tao, J. Chen, *Adv. Funct. Mater.* **2015**, 25, 214.
- [21] Y. Liu, N. Zhang, L. Jiao, J. Chen, *Adv. Mater.* **2015**, 27, 6702.
- [22] Y. Guo, X. Zeng, Y. Zhang, Z. Dai, H. Fan, Y. Huang, W. Zhang, H. Zhang, J. Lu, F. Huo, Q. Yan, *ACS Appl. Mater. Interfaces* **2017**, 9, 17172.
- [23] M. Sha, H. Zhang, Y. Nie, K. Nie, X. Lv, N. Sun, X. Xie, Y. Ma, X. Sun, *J. Mater. Chem. A* **2017**, 5, 6277.
- [24] C. Wu, P. Kopold, P. A. van Aken, J. Maier, Y. Yu, *Adv. Mater.* **2017**, 29, 1604015.
- [25] S.-O. Kim, A. Manthiram, *Chem. Commun.* **2016**, 52, 4337.
- [26] M. Fan, Y. Chen, Y. Xie, T. Yang, X. Shen, N. Xu, H. Yu, C. Yan, *Adv. Funct. Mater.* **2016**, 26, 5019.
- [27] W. Li, L. Ke, Y. Wei, S. Guo, L. Gan, H. Li, T. Zhai, H. Zhou, *J. Mater. Chem. A* **2017**, 5, 4413.
- [28] W. Qi, H. Zhao, Y. Wu, H. Zeng, T. Tao, C. Chen, C. Kuang, S. Zhou, Y. Huang, *Sci. Rep.* **2017**, 7, 43582.
- [29] W.-J. Li, S.-L. Chou, J.-Z. Wang, H.-K. Liu, S.-X. Dou, *Chem. Commun.* **2015**, 51, 3682.
- [30] Z. Li, L. Zhang, X. Ge, C. Li, S. Dong, C. Wang, L. Yin, *Nano Energy* **2017**, 32, 494.
- [31] X. Fan, J. Mao, Y. Zhu, C. Luo, L. Suo, T. Gao, F. Han, S.-C. Liou, C. Wang, *Adv. Energy Mater.* **2015**, 5, 1500174.
- [32] H. Usui, Y. Domi, K. Fujiwara, M. Shimizu, T. Yamamoto, T. Nohira, R. Hagiwara, H. Sakaguchi, *ACS Energy Lett.* **2017**, 2, 1139.
- [33] D. Lan, W. Wang, L. Shi, Y. Huang, L. Hu, Q. Li, *J. Mater. Chem. A* **2017**, 5, 5791.
- [34] W. Li, S.-L. Chou, J.-Z. Wang, J. H. Kim, H.-K. Liu, S.-X. Dou, *Adv. Mater.* **2014**, 26, 4037.
- [35] J. Qian, Y. Xiong, Y. Cao, X. Ai, H. Yang, *Nano Lett.* **2014**, 14, 1865.
- [36] J. Liu, P. Kopold, C. Wu, P. A. van Aken, J. Maier, Y. Yu, *Energy Environ. Sci.* **2015**, 8, 3531.
- [37] Y. Kim, Y. Kim, A. Choi, S. Woo, D. Mok, N.-S. Choi, Y. S. Jung, J. H. Ryu, S. M. Oh, K. T. Lee, *Adv. Mater.* **2014**, 26, 4139.
- [38] J. Y. Jang, Y. Lee, Y. Kim, J. Lee, S.-M. Lee, K. T. Lee, N.-S. Choi, *J. Mater. Chem. A* **2015**, 3, 8332.
- [39] H.-S. Shin, K.-N. Jung, Y. N. Jo, M.-S. Park, H. Kim, J.-W. Lee, *Sci. Rep.* **2016**, 6, 26195.
- [40] L. Ma, P. Yan, S. Wu, G. Zhu, Y. Shen, *J. Mater. Chem. A* **2017**, 5, 16994.
- [41] L. Zheng, R. A. Dunlap, M. N. Obrovac, *J. Electrochem. Soc.* **2016**, 163, A1188.
- [42] V. Tallapally, R. J. A. Esteves, L. Nahar, I. U. Arachchige, *Chem. Mater.* **2016**, 28, 5406.
- [43] L. Häggström, J. Gullman, T. Ericsson, R. Wäppling, *J. Solid State Chem.* **1975**, 13, 204.
- [44] A. V. Naumkin, A. Kraut-Vass, S. W. Gaarenstroom, C. J. Powell, *NIST X-Ray Photoelectron Spectroscopy Database*, National Institute of Standards and Technology (NIST), Gaithersburg, U.S.A., **2012**.
- [45] J. Sun, H.-W. Lee, M. Pasta, Y. Sun, W. Liu, Y. Li, H. R. Lee, N. Liu, Y. Cui, *Energy Storage Mater.* **2016**, 4, 130.
- [46] J. Song, Z. Yu, M. L. Gordin, X. Li, H. Peng, D. Wang, *ACS Nano* **2015**, 9, 11933.
- [47] Z. Yu, J. Song, M. L. Gordin, R. Yi, D. Tang, D. Wang, *Adv. Sci.* **2015**, 2, 1400020.
- [48] G. Peters, I. Thede, V. Vill, R. Zenczykowski, *Landolt-Börnstein Substance/Property Index*, LCI Publisher GmbH, Hamburg, Germany, **2009**.
- [49] J. Sun, G. Zheng, H.-W. Lee, N. Liu, H. Wang, H. Yao, W. Yang, Y. Cui, *Nano Lett.* **2014**, 14, 4573.
- [50] J. Sangster, C. W. Bale, *J. Phase Equilib. Diffus.* **1998**, 19, 76.
- [51] L. Baggetto, P. Ganesh, R. P. Meisner, R. R. Unocic, J.-C. Jumas, C. A. Bridges, G. M. Veith, *J. Power Sources* **2013**, 234, 48.
- [52] L. D. Ellis, T. D. Hatchard, M. N. Obrovac, *J. Electrochem. Soc.* **2012**, 159, A1801.
- [53] Z. Du, R. A. Dunlap, M. N. Obrovac, *J. Alloys Compd.* **2014**, 617, 271.
- [54] M. K. Datta, R. Epur, P. Saha, K. Kadakia, S. K. Park, P. N. Kumta, *J. Power Sources* **2013**, 225, 316.
- [55] M. Dahbi, N. Yabuuchi, M. Fukunishi, K. Kubota, K. Chihara, K. Tokiwa, X.-f. Yu, H. Ushiyama, K. Yamashita, J.-Y. Son, Y.-T. Cui, H. Oji, S. Komaba, *Chem. Mater.* **2016**, 28, 1625.
- [56] Y.-U. Kim, C. K. Lee, H.-J. Sohn, T. Kang, *J. Electrochem. Soc.* **2004**, 151, A933.
- [57] H. Lu, B. Xu, J. Shi, M. Wu, Y. Hu, C. Ouyang, *Mod. Phys. Lett. B* **2016**, 30, 1650385.